EXTENDED MOODY DIAGRAM FOR WALL MODELED LARGE EDDY SIMULATION INCLUDING UNRESOLVED NEAR WALL SEPARATION

Ho Jun Kim
Department of Mechanical Engineering
Johns Hopkins University
Baltimore, MD 21218, USA
hkim324@jhu.edu

Tamer A. Zaki
Department of Mechanical Engineering
Johns Hopkins University
Baltimore, MD 21218, USA
t.zaki@jhu.edu

Charles Meneveau
Department of Mechanical Engineering
Johns Hopkins University
Baltimore, MD 21218, USA
meneveau@jhu.edu

ABSTRACT

Traditional equilibrium wall models for large eddy simulation (LES) typically assume that the wall shear stress is aligned with the LES velocity at the wall-model matching height. While this assumption works reasonably well in attached boundary layers, it breaks down in separated flows when the matching point lies above a near-wall region of reversed flow. Existing wall models are not designed to handle this situation when the separation is unresolved and caused by strong adverse pressure gradients. In this work, we extend the Moody-diagram-based wall model so that it can account for velocity profiles exhibiting near-wall flow reversal. Rather than solving the associated ordinary differential equations iteratively during the simulation, we solve them offline and construct accurate fitting functions. These fits span the parameter range relevant to unresolved reverse flow, including cases with strong adverse pressure gradients and low-to-moderate local Reynolds numbers. We assess the performance of the extended wall model for LES of turbulent flow over periodic hills, a canonical test case featuring local separation. The extended model provides improved wall-stress predictions in regions where small, unresolved separation regions exist below the matching height.

INTRODUCTION

Wall-modeled large-eddy simulation (WMLES) reduces computational cost by modeling the near-wall physics and providing the wall stress as a boundary condition (Piomelli, 2008). The classic equilibrium wall model integrates the boundary layer equation in the wall-normal direction assuming the equilibrium conditions, at every time-step and grid-point along the surface. The equation has the form of an ordinary differential equation as a boundary value problem for the wall stress, given the LES velocity at the wall model matching location. To avoid iterative numerical procedures for solving this boundary value problem at every grid point on the wall and timestep during LES, the properly normalized local boundary layer equations were solved numerically once, and results fitted, yielding a generalized Moody-diagram (GMD) wall model (Meneveau, 2020). The method included effects of pressure gradient as well as wall roughness. Given the Reynolds number and a pressure gradient parameter defined by LES variables available at the wall model height above the wall, the precomputed fits allowed obtaining a wall-model friction factor, from which the local wall stress could be computed and used in LES. The GMD model was also used in LES of rough wall boundary layers (Salomone *et al.* 2025). Effects of favorable and adverse pressure gradient were included, but only up to separation. As in all classical wall models, the approach assumed that the wall stress is in the same direction as the input LES velocity at the wall model matching location. Therefore, its corresponding wall model Moody diagram (Meneveau, 2020) only described positive skin friction coefficients.

To address limitations of prior wall models, in this work we include the possibility of near-wall reversed velocity profiles in response to strong adverse pressure gradient and extend the Moody diagram approach to include negative friction factor regimes. The extended generalized Moody diagram (eGMD) wall model is implemented in LES of turbulent flow over periodic hills, including separation, and the effects of including or not including reverse flow conditions are documented.

EXTENDEDED GENERALIZED MOODY DIAGRAM

The relation between wall shear stress and LES inputs at the wall model matching location can be derived from the non-equilibrium boundary layer equation, which accounts for the effect of the streamwise pressure gradient

$$\frac{d}{dy}\left((\nu+\nu_t)\frac{du}{dy}\right)=\frac{\partial p}{\partial x} \tag{1}$$

where x is aligned with the wall parallel LES velocity u at the matching location Δ, y is aligned with the local wall normal direction and p is pressure divided by density. The eddy viscosity is modeled using the mixing length model $\nu_t = (D(y)\kappa y)^2|du/dy|$, where $D(y)$ is a wall-damping function.

Upon integration of Eq. (1) from $y = 0$ to some arbitrary height y, and nondimensionalizing with available parameters known a-priori (Δ and ν), the momentum balance reads:

$$\left(1+(D\kappa y')\left|\frac{du'}{dy'}\right|\right)\frac{du'}{dy'}=\psi_p y'+\zeta Re_{\tau\Delta}^2 \tag{2}$$

where $y' = y/\Delta$, $u' = u\Delta/\nu$, $\psi_p = \frac{dp}{dx}\frac{\Delta^3}{\nu^2}$, $Re_{\tau\Delta} = \frac{u_{\tau\Delta}\Delta}{\nu}$, with $u_{\tau\Delta}$ being the local friction velocity, and Δ is the wall model height. The ζ on the right-hand side of equation is: $\zeta = 1$ for unidirectional flow or $\zeta = -1$ for near-wall reversed flow. Eq. (2) is numerically integrated up to $y' = 1$ to obtain $Re_\Delta = \frac{U_{LES}\Delta}{\nu}$. The damping function with pressure correction proposed by Cebeci (1970) is slightly modified here to avoid unphysical behavior near the separation point. By integrating Eq. (2), the velocity u_Δ at the matching location Δ is obtained. Representative velocity profiles are shown in Figure 1.

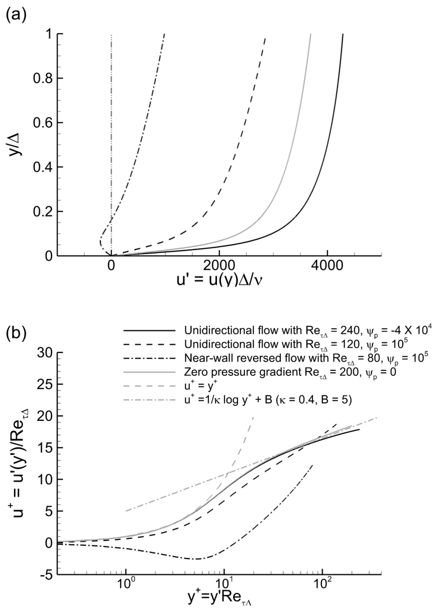

Figure 1. Velocity profiles obtained from numerical integration at various $Re_{\tau\Delta}$ under zero ($\psi_p = 0$), favorable ($\psi_p = -4 \times 10^4$) and adverse ($\psi_p = 10^5$) pressure gradients. The resulting Re_Δ values $u'(1)$ were 3.69×10^3 $(Re_{\tau\Delta} = 200,\ \psi_p = 0)$, 4.29×10^3 $(Re_{\tau\Delta} = 240,\ \psi_p = -4 \times 10^4)$, 2.87×10^3 ($Re_{\tau\Delta} = 120,\ \psi_p = 10^5$, unidirectional), and 9.83×10^2 ($Re_{\tau\Delta} = 80,\ \psi_p = 10^5$, near-wall reversed). (a) linear scale (b) semi-log scale plot in the wall unit. The linear and logarithmic velocity profiles are indicated by grey dashed and dash-dotted lines, respectively.

It should be noted that only the non-reversed case $\zeta = 1$ was considered in Meneveau (2020) to obtain the fitting function (denoted there as $Re_{\tau\Delta}^{pres}$). Therefore, the possibility of near-wall reversed velocity profile was not included.

To determine the wall stress corresponding to a given LES velocity and pressure gradients, the ordinary differential equation must be solved iteratively. For efficient computation of wall shear stress, the numerically integrated results are approximated by fitting functions. In the construction of these functions, asymptotic analytical expressions are formulated, and different asymptotic functional forms are smoothly connected. The parameters bridging different forms are optimized to minimize errors in the resulting wall modelling skin friction coefficient $c_f^{wm}(Re_\Delta, \psi_p) = 2\zeta(Re_{\tau\Delta}/Re_\Delta)^2$. During LES, from the skin friction coefficient, the wall shear stress can be computed as

$$\tau_w = \frac{1}{2}\rho u_\Delta^2 c_f^{wm}(Re_\Delta, \psi_p) \qquad (3)$$

For zero pressure gradient cases, $\psi_p = 0$, the fitting function c_f^{wm} in eq. (3) is given by Meneveau (2020):

$$c_f^{wm} = \kappa_4^2 Re_\Delta^{2(\beta_1-1)}\left[1 + (\kappa_3 Re_\Delta)^{-\beta}\right]^{(2\beta_1-1)/\beta_2}$$

where

$$\beta_1 = \left[1.0 + \frac{0.155}{Re_\Delta^{0.03}}\right]^{-1.0}, \beta_2 = 1.7 - \left[1.0 + \frac{36.0}{Re_\Delta^{0.75}}\right]^{-1.0},$$
$$\kappa = 0.4, \kappa_3 = 0.005, \kappa_4 = \kappa_3^{\beta_1 - 1/2}$$

Additional ingredients for the fitting function accounting for pressure gradient effects depend on the pressure gradient parameter ψ_p and on 27 additional empirically optimized parameters. The expressions are presented in Kim *et al.* (2026).

The numerically integrated wall model friction coefficient is compared with the fitting function in Figure 2. The fitting function shows excellent agreement with the numerical result over a wide range of Reynolds numbers and pressure gradient parameters. And, as can be seen, this eGMD wall model version contains a negative part.

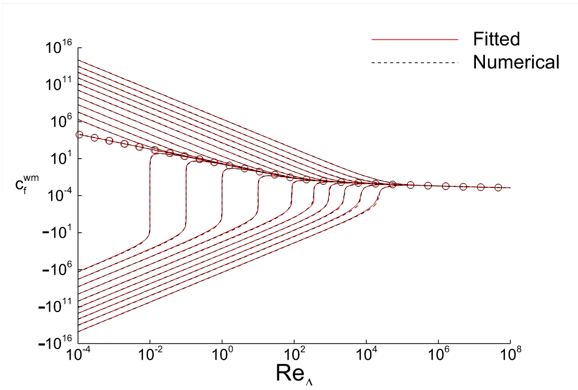

Figure 2. The extended Moody's diagram including negative part, with fitting function and numerically integrated results for (from bottom to top): $\psi_p = 2 \times 10^7, 2 \times 10^6, 2 \times 10^5, \ldots\ldots 20, 2, 0.2, 0.02, 0, -0.02, -0.2, -2, -20, -2 \times 10^2, -2 \times 10^3, -2 \times 10^4, -2 \times 10^5, -2 \times 10^6, -2 \times 10^7$. Dashed lines show the numerically obtained results and solid lines denote the constructed fitting functions. The circles highlight the zero-pressure gradient baseline case.

In the next section, we compare the performance of three variants of GMD wall models in a flow with mean separation: 1. Equilibrium wall model without pressure gradient correction term, i.e. using $c_f^{wm} = c_f^{wm}(Re_\Delta, \psi_p = 0)$; 2. GMD wall model with pressure gradient correction but without near-wall reversed flow, i.e. using $c_f^{wm} = \max(0, \zeta)\, c_f^{wm}(Re_\Delta, \psi_p)$; 3. Full eGMD wall model $c_f^{wm} = c_f^{wm}(Re_\Delta, \psi_p)$ with pressure gradient correction and including the possibility of near-wall reverse flow.

APPLICATION TO FLOW OVER PERIODIC HILLS

After testing the model in standard equilibrium channel flow with results (Kim *et al.,* 2026) equivalent to those of the traditional equilibrium wall model (as expected), the turbulent flow over periodic hills (Fröhlich *et al.* 2005; Rapp et al. 2010, Gloerfelt and Cinnella 2019) was selected as a highly relevant test case. This flow is characterized by a large flow separation on the leeward side of the hill, followed by reattachment and a recovery region. The computational domain was discretized using a curvilinear structured grid. Time integration of incompressible Navier-Stokes equation was performed with a fractional step method. The Adams-Bashforth scheme was employed for the convective and explicit diffusion terms, while the Crank-Nicolson scheme was used for the implicit diffusion terms. Fully implicit Euler method was used for pressure terms. The multi-grid method was used to solve the Fourier transformed Poisson equation in the spanwise direction. Further details of the numerical implementation are provided in Lee and Zaki (2018). For the subgrid scale (SGS) model, the mixed model (Liu, Meneveau, and Katz, 1994) was used with the dynamic Smagorinsky model of Germano *et al.* (1991) as the eddy viscosity part. The resulting SGS stress modeled by the mixed model is expressed as: $\boldsymbol{\tau}^{SGS} = -2\left(c_s\Delta^{filt}\right)^2|\tilde{\boldsymbol{S}}|\tilde{\boldsymbol{S}} + \left(\overline{\tilde{\boldsymbol{u}}\tilde{\boldsymbol{u}}} - \bar{\tilde{\boldsymbol{u}}}\,\bar{\tilde{\boldsymbol{u}}}\right)$ where $\bar{\cdot}$ and $\tilde{\cdot}$ denotes the horizontal box-filtered value with filter sizes $2\Delta^{filt}$ and Δ^{filt} (the grid size) respectively. The Smagorinsky constant c_s in the eddy viscosity portion was dynamically determined by the dynamic model, spanwise averaging and clipping occasional negative values. Periodic boundary conditions were applied in the streamwise and spanwise directions. At the top and bottom boundaries, the wall stress was prescribed using wall models based on three wall models: equilibrium, GMD and eGMD wall models. In the following sections, x, y, and z denote the Cartesian coordinates in the horizontal, vertical, and spanwise directions and corresponding velocities are denoted as u, v, and w. The computational domain size follows Fröhlich *et al.* (2005), namely $\left(L_x, L_y, L_z\right) = (9.0, 3.035, 4.5)h_{max}$ where h_{max} is the hill height. The Reynolds number, defined using the hill height and bulk velocity at the hill crest $U_b = \frac{1}{3.035-1}\int_{1.0}^{3.035} u(y)dy$, was set to 37,000. The domain was discretized with an approximately uniform grid of $193 \times 97 \times 97$ points as shown in Fig. 3. Two separate applications are compared, with wall model input values extracted from either the second or third grid points from the wall.

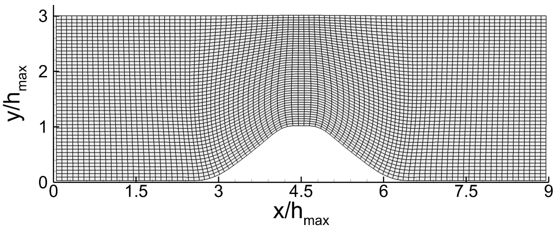

Figure 3. Computational grid showing each second line.

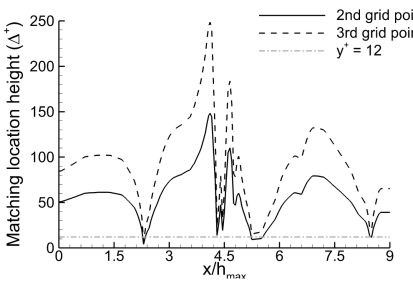

Figure 4. Matching location heights Δ in wall units for the second grid point (black solid line) and third grid point (black dashed line). The grey dash-dotted horizontal line denotes $y^+ = 12$.

The corresponding matching location heights are shown in Figure 4 in inner units, using the reference wall-resolved large eddy simulation (WRLES) friction velocity at every point. In most of the domain, the matching location lies significantly above the viscous sublayer height $l_s^+ = 12$ of a canonical turbulent near-wall flow.

The wall stress distribution obtained from LES is compared in Figure 5 to WRLES results from the literature (Gloerfelt and Cinnella, 2019). The equilibrium wall model without pressure gradient correction shows a delayed and smaller peak compared to WRLES. Conversely, the first peak is better predicted by the other two wall models that include a pressure gradient correction term. This result illustrates that the pressure gradient effect is significant in the windward side of the hill. In the favorable pressure gradient region, both GMD and eGMD wall models show identical result as both models are equivalent in the favorable pressure gradient part.

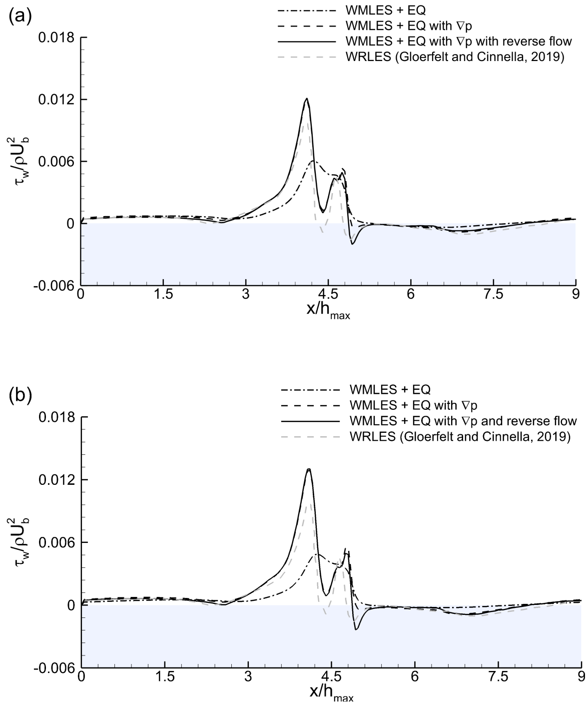

Figure 5. Comparison of wall shear stress for different wall models: the equilibrium (dash-dotted line), GMD (dashed line), and eGMD (solid line) wall models. The reference WRLES result is the grey dashed line. The negative wall shear stress region is shaded by light blue color. (a) second grid point (b) third grid point matching locations

To investigate the effect of near wall reverse flow part in the eGMD wall model, the incipient flow separation region $x/h_{max} = 4.94$ is shown in Figure 6. Since in our WMLES the matching location height lies above the near-wall reverse flow region, the equilibrium and clipped GMD wall models yield positive wall shear stress when the LES velocity is forward. They therefore predict longer attached flow and positive wall shear stress further downstream. On the other hand, the eGMD wall model with reversed flow displays earlier flow separation closer to the reference WRLES result.

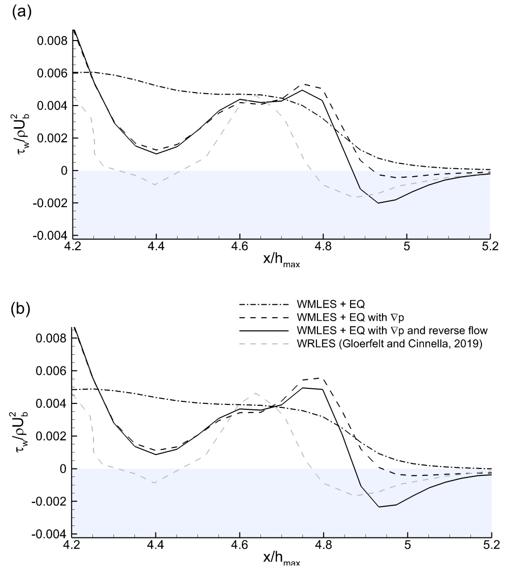

Figure 6. Predicted wall shear stress near the separation with different wall models (same legends as Figure 5). (a) second grid point (b) third grid point matching locations

Sample time histories of local friction Reynolds number and wall model friction factor in the incipient flow separation region at $x/h_{max} = 4.94$ are shown in Figure 7. At this location, the equilibrium wall model remains positive, while the GMD wall model has negative portion clipped to zero. With the negative part of the diagram, the eGMD wall model displays strong temporal fluctuations over negative and positive values. The slight negative friction factor is the result of averaging over both positive and negative contributions.

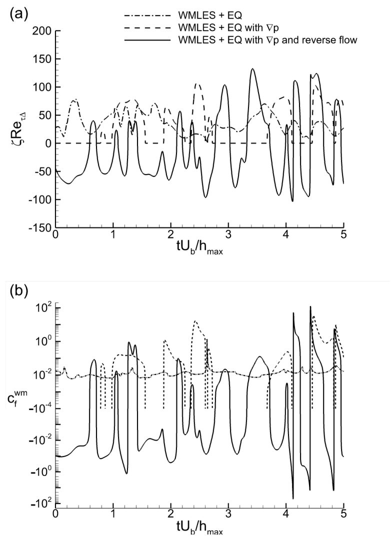

Figure 7. (a) The time history of local friction Reynolds number $\zeta Re_{\tau\Delta}$ at $x/h_{max} = 4.94$ and an arbitrary spanwise location $z/h_{max} = 4.94$ with different wall models: the equilibrium (dash-dotted line), GMD (dashed line), and eGMD (solid line) wall models (b) Same as (a) as expressed in terms of the wall model friction factor c_f^{wm}, and in logarithmic units

The pressure gradient dominant part (left side of Figure 2) appears as peaks in the wall model skin friction factor for GMD and eGMD wall models with the pressure gradient correction term. The same time history of wall friction factor is plotted on the extended generalized Moody diagram in Figure 8**.** As expected, the equilibrium wall model without pressure gradient correction term follows the single zero pressure gradient line highlighted with the circles. The wall model skin friction factor from GMD and eGMD wall models with pressure gradient correction moves across the various lines representing different pressure gradient parameters. The negative skin friction factor is clipped to zero in GMD wall model and appeared as discontinued vertical lines while the vertical lines are smoothly connected to the negative part in the eGMD wall model.

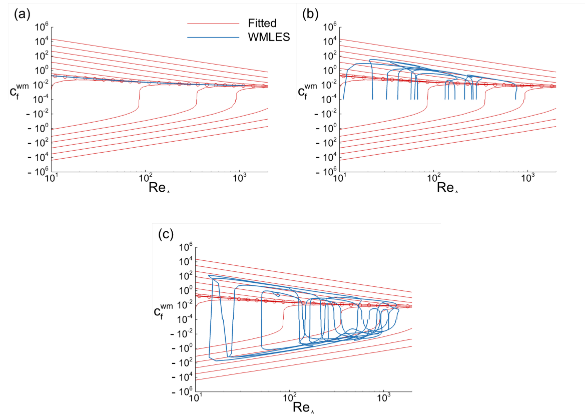

Figure 8. Wall model friction factor from Figure 7 by thick blue solid line, overlaid on the extended generalized Moody diagram for different wall models: (a) the equilibrium, (b) GMD, and (c) eGMD wall models

Further insights into wall model characteristics are provided by comparing the velocity profiles extended from the LES domain all the way towards the wall. For illustrative purposes, the numerical integration for the velocity profile at a selected point near the hill crest using the LES inputs is performed. At this location, the mean pressure gradient is slightly adverse. The resulting time-averaging and instantaneous velocity profiles are shown in Figure 9. The subscript t denotes the wall tangential direction as this is the velocity component subsumed by the wall model. Both GMD and eGMD wall models follow the WRLES velocity profiles in this region with the pressure gradient correction term. The equilibrium wall model shows fuller velocity profiles since it does not account for the slight adverse pressure gradient effect in this region. This results in the overprediction of wall shear stress near the hill crest at $x/h_{max} = 4.4$ as shown in Figure 5. Panel (b) shows the numerically obtained instantaneous velocity profiles using the instantaneous LES inputs at the wall model matching location height (red dashed line). In the LES region above the matching location linear interpolation is used but towards the wall, the ODE solution is shown. Strong fluctuations are evident in the instantaneous velocity profiles.

To illustrate the performance of the eGMD wall model in the region where the near-wall reverse flow appears, the velocity profiles obtained from integrating the ODE near the separation point ($x/h_{max} = 4.8$) are shown in Figure 10. For the equilibrium wall model without considering adverse pressure gradient in this region exhibits fuller velocity profile with a higher wall shear stress. Incorporating pressure gradient effect in the GMD wall model improves the velocity profile results but the flow separation is not captured with the missing negative wall shear stress part by the clipping. Unresolved flow separation below the matching location is predicted when using the eGMD model that includes the near-wall reversed flow velocity profiles. However, the reverse flow part of the eGMD wall model is limited to a rather small near-wall region while the WRLES generates a more strongly separated flow.

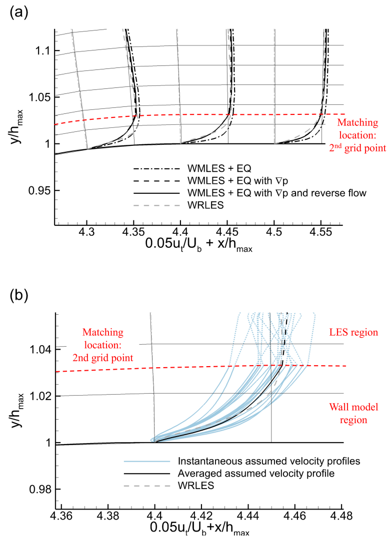

Figure 9. Mean and instantaneous velocity profiles below the matching location and LES velocity profiles above matching location near the hill crest (a) Mean velocity profiles with different wall models: the equilibrium (black dash-dotted line), the GMD (black dashed line), and eGMD (black solid line) wall models. The WRLES result is indicated by the grey solid line. (b) Mean (black line) and instantaneous (light blue) velocity profiles from eGMD wall model and mean WRLES velocity profiles (grey line) at $x/h_{max} = 4.4$. Solid line indicates the assumed velocity profile in the wall model region, while dotted lines represent the LES velocity.

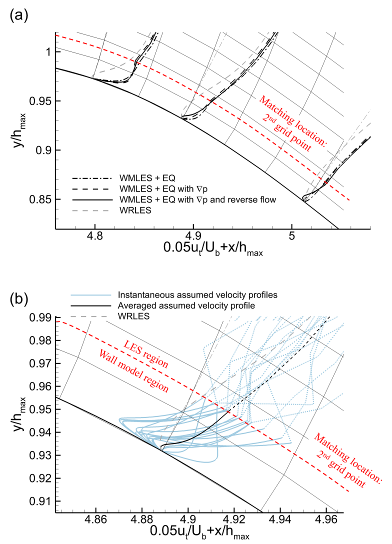

Figure 10. Mean and instantaneous velocity profiles below the matching location and LES velocity profiles above matching location near the separation point (same legends as Figure 9). In (b) the model is the eGMD wall model.

All wall models overpredict the mean velocity in the LES region and massive separation occurs later than the WRLES reference data. The instantaneous velocity profiles from eGMD wall model are shown in panel (b). Strong variability at this near separation point appears, but the overall averaged velocity profile shows only a small reverse flow region.

The overall temporal and spatial evolution of wall model input Reynolds number, pressure gradient parameter, and the wall model output friction Reynolds number are shown in Figure 11.

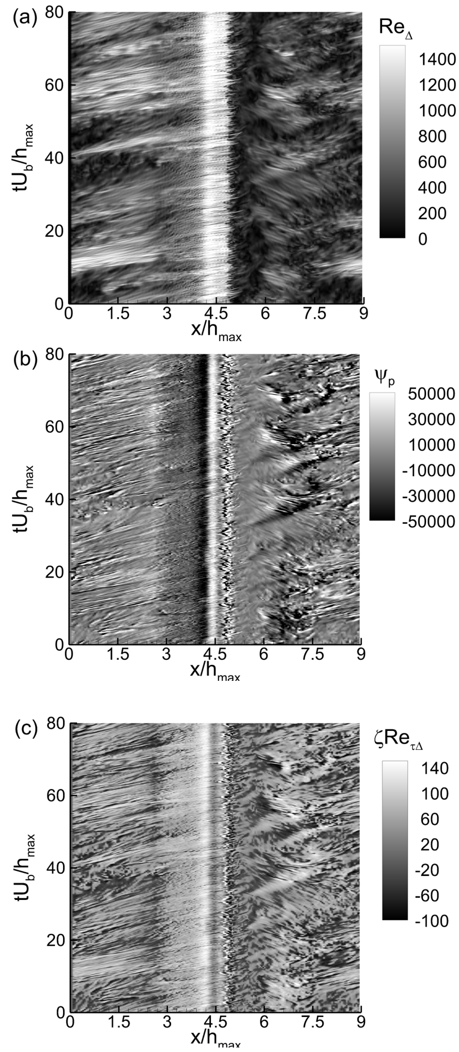

Figure 11. Spatial and temporal changes of (a) wall model input Reynolds number Re_{Δ}, (b) pressure gradient parameter ψ_p, and (c) wall model friction Reynolds number $Re_{\tau\Delta}$ along an arbitrary spanwise line at $z/h_{max} = 2.25$, and using the second grid point in the eGMD wall modeled LES.

In the windward side of the hill, $3.0 \leq x/h_{max} \leq 4.2$, the flow is accelerated by a favorable pressure gradient showing a high input Reynolds number (bright region in Figure 11 (a)) and large negative pressure gradient parameter (dark region in Figure 11 (b)). The favorable pressure gradient is followed by an adverse pressure gradient region $4.2 \leq x/h_{max} \leq 4.6$. However, the LES velocity, thus input Reynolds number, still shows large values in this adverse pressure gradient region. Therefore, the equilibrium wall model without a pressure gradient correction overpredicts the wall shear stress in this region, as shown in Figure 5. In the following flow separation and recovery regions, input wall model Reynolds number is low; however, the pressure gradient parameter shows intermittent large favorable and adverse pressure gradient values. The output wall model friction Reynolds number is anti-correlated with the pressure gradient parameter at this low LES velocity region. Another observation is that all the variables advect downstream faster in the windward side of the hill and become slower in the flow separation recovery regions. The flow separation region shows upstream advection with reverse flow occurs inside the separation bubble. Advective behavior of the wall stress was considered explicitly in the Lagrangian relaxation towards equilibrium wall model framework by Fowler *et al.* (2023) and its extensions to rough surfaces by Salomone *et al.* (2026). Figure 12 near $6 \leq x/h_{max} \leq 7.5$ also displays very long-timescale breathing behavior, as is known to occur in separation bubbles.

In Figure 12, the streamwise velocity profiles are compared with WRLES data from Gloerfelt and Cinnella (2019) and experimental measurements from Rapp et al. (2010). The differences in wall shear stress are found to have negligible effects on the streamwise velocity profiles. All wall models considered show good agreement with the WRLES and experimental velocity profile results, including the equilibrium wall model which predicts a wall shear stress distribution that deviates from that of WRLES. It was found that the sub-grid scale model and discretization method have more significant effects on the velocity field (Kim *et al.,* 2026).

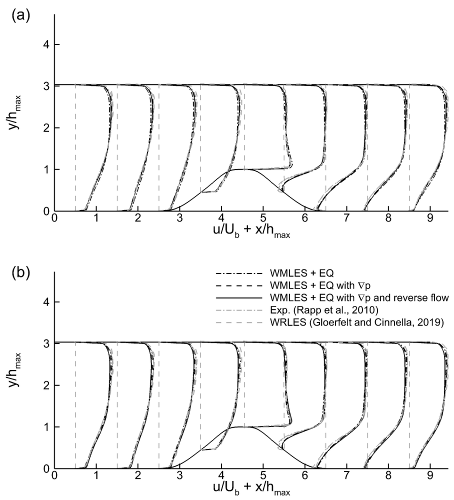

Figure 12. Streamwise velocity profiles at various streamwise locations x/h_{max} for different wall models: the equilibrium (dash-dotted line), GMD (dashed line), and eGMD (solid line) wall models. The reference experimental and WRLES results are indicated by the grey dash-dotted and dashed lines, respectively. WMLES used (a) second grid point (b) third grid point matching locations

CONCLUSIONS

The missing negative wall stress part of Moody's diagram has been incorporated in the eGMD wall model by allowing for velocity profiles with near-wall reversed flow. To enable efficient evaluation of friction factor and wall stress, a fitting function approach was adopted. The generated fitting function generalizes and improves on the GMD wall model given in Meneveau (2020) with an extension including the near wall reversed flow. The eGMD wall model was applied to the turbulent flow over periodic hills reference case, at a bulk flow Reynolds number of 37,000. In the data, near-wall reverse flow in the incipient flow separation region would be located below the matching location in coarse-grid LES, as is typical in WMLES. In that region, the eGMD wall model shows improved (but not perfect) agreement with data compared to the equilibrium and GMD wall models that did not account for the near-wall reversed flow. The improved agreement was traced to intermittent near-wall reversed flow as observed in time histories of wall stress and inclusion of the velocity profiles with near-wall reversed flow. The spatial and temporal changes of wall model input values illustrate the importance of pressure gradient effects in this flow configuration, as well as the advective character of the wall stress spatio-temporal evolution. For streamwise velocity profiles, we found that the effects of SGS modeling are much more significant than the wall model choice. If appropriate grid spacing and SGS model was used, we found that all considered wall models yielded good agreement with the reference data for the streamwise velocity profiles in this flow.

Other separated flows as well as the multiple-time scale method (Fowler *et al.* 2023) will be explored in combination with the eGMD wall model in future work.

This research was supported by the Office of Naval Research, project N00014-23-12185. This work was carried out at the Advanced Research Computing at Hopkins (ARCH) core facility (rockfish.jhu.edu), which is supported by the National Science Foundation (NSF) grant number OAC 1920103.

REFERENCES

Fowler, M., Zaki, T.A. and Meneveau, C., 2023, "A multi-time-scale wall model for LES and applications to non-equilibrium channel flows", *J. Fluid Mech.* **974**, A51.

Fröhlich, J., Mellen, C. P., Rodi, W., Temmerman, L., and Leschziner, M., A., 2005, "Highly resolved large-eddy simulation of separated flow in a channel with streamwise periodic constrictions", *J. Fluid Mech.*, **526**, 19-66.

Germano, M., Piomelli U., Moin P., and Cabot W. H., 1991, "A dynamic subgrid-scale eddy viscosity model", *Phys. Fluids* **3**, 1760-1765.

Gloerfelt, X., and Cinnella, P., 2019, "Large Eddy Simulation Requirements for the Flow over Periodic Hills", *Flow, Turbulence and Combustion*, Vol. 103, 55-91.

Kim, H. J., Zaki, T. A., and Meneveau, C., 2026, "Extended Moody diagram for wall-modeled LES accounting for near-wall reversed flow" (*in preparation).*

Lee, J., and Zaki, T. A., 2018, "Detection algorithm for turbulent interfaces and large-scale structures in intermittent flows", *Computers and Fluids*, **175**, 142-158.

Liu, S., Meneveau, C., and Katz, J., 1994, "On the properties of similarity subgrid-scale models as deduced from measurements in a turbulent jet", *J. Fluid Mech.*, **275**, 83-119.

Meneveau, C., 2020, "A note on fitting a generalised Moody diagram for wall modelled large-eddy simulations", *J. Turbulence*, **21**, 650–673.

Piomelli, U., 2008, Wall-layer models for large-eddy simulations. Prog. Aerosp. Sci. **44**, 437–446.

Rapp., C., Breuer, M., Manhart, M., and Peller, N. 2009, updated 2013, "UFR 3-30 Test Case", *ERCOFTAC.*

Salomone, T., Meneveau, C., De Stefano, G., and Piomelli, U. 2025 "Wall-model response to departure from equilibrium in turbulent flows over rough surfaces", *J. Fluid Mech.* **1023**, A16.